

Substantial cooling effect from aerosol-induced increase in tropical marine cloud cover

Article

Published Version

Creative Commons: Attribution 4.0 (CC-BY)

Open Access

Chen, Y. ORCID: <https://orcid.org/0000-0002-0319-4950>,
Haywood, J. ORCID: <https://orcid.org/0000-0002-2143-6634>,
Wang, Y. ORCID: <https://orcid.org/0000-0002-9480-3570>,
Malavelle, F., Jordan, G. ORCID: <https://orcid.org/0000-0002-3129-4983>, Peace, A., Partridge, D. G. ORCID:
<https://orcid.org/0000-0002-5970-901X>, Cho, N. ORCID:
<https://orcid.org/0000-0001-6401-2391>, Oreopoulos, L.
ORCID: <https://orcid.org/0000-0001-6061-6905>, Grosvenor, D.,
Field, P., Allan, R. P. ORCID: <https://orcid.org/0000-0003-0264-9447> and Lohmann, U. ORCID: <https://orcid.org/0000-0001-8885-3785> (2024) Substantial cooling effect from aerosol-induced increase in tropical marine cloud cover. *Nature Geoscience*, 17. pp. 404-410. ISSN 1752-0908 doi: 10.1038/s41561-024-01427-z Available at <https://centaur.reading.ac.uk/116007/>

It is advisable to refer to the publisher's version if you intend to cite from the work. See [Guidance on citing](#).

To link to this article DOI: <http://dx.doi.org/10.1038/s41561-024-01427-z>

All outputs in CentAUR are protected by Intellectual Property Rights law, including copyright law. Copyright and IPR is retained by the creators or other copyright holders. Terms and conditions for use of this material are defined in the [End User Agreement](#).

www.reading.ac.uk/centaur

CentAUR

Central Archive at the University of Reading

Reading's research outputs online



Substantial cooling effect from aerosol-induced increase in tropical marine cloud cover

Received: 24 August 2023

Accepted: 20 March 2024

Published online: 11 April 2024

Ying Chen ^{1,2}✉, Jim Haywood ^{2,3}, Yu Wang ^{4,5}, Florent Malavelle ⁶, George Jordan ³, Amy Peace ^{2,3}, Daniel G. Partridge ², Nayeong Cho ^{7,8}, Lazaros Oreopoulos ⁷, Daniel Grosvenor ^{3,9}, Paul Field ^{9,10}, Richard P. Allan ¹¹ & Ulrike Lohmann ⁵

Check for updates

With global warming currently standing at approximately +1.2 °C since pre-industrial times, climate change is a pressing global issue. Marine cloud brightening is one proposed method to tackle warming through injecting aerosols into marine clouds to enhance their reflectivity and thereby planetary albedo. However, because it is unclear how aerosols influence clouds, especially cloud cover, both climate projections and the effectiveness of marine cloud brightening remain uncertain. Here we use satellite observations of volcanic eruptions in Hawaii to quantify the aerosol fingerprint on tropical marine clouds. We observe a large enhancement in reflected sunlight, mainly due to an aerosol-induced increase in cloud cover. This observed strong negative aerosol forcing suggests that the current level of global warming is driven by a weaker net radiative forcing than previously thought, arising from the competing effects of greenhouse gases and aerosols. This implies a greater sensitivity of Earth's climate to radiative forcing and therefore a larger warming response to both rising greenhouse gas concentrations and reductions in atmospheric aerosols due to air quality measures. However, our findings also indicate that mitigation of global warming via marine cloud brightening is plausible and is most effective in humid and stable conditions in the tropics where solar radiation is strong.

Aerosol-induced increases in liquid cloud opacity cool the Earth by enhancing reflection of sunlight back to space and offset a large, yet poorly quantified, portion of greenhouse gas warming¹. The climate impacts of aerosol–cloud interactions (ACI) have been widely

debated in the past few decades and still constitute one of the largest uncertainties in the estimate of radiative forcing^{1–3}, impeding a better understanding of climate sensitivity⁴ and the remaining carbon emissions budget for avoiding overshooting the +1.5 °C

¹School of Geography, Earth and Environmental Sciences, University of Birmingham, Birmingham, UK. ²Department of Mathematics and Statistics, Faculty of Environment, Science and Economy, University of Exeter, Exeter, UK. ³Met Office Hadley Centre, Exeter, UK. ⁴School of GeoSciences, University of Edinburgh, Edinburgh, UK. ⁵Institute for Atmospheric and Climate Science, ETH Zurich, Zurich, Switzerland. ⁶Met Office, Exeter, UK. ⁷Earth Sciences Division, NASA GSFC, Greenbelt, MD, USA. ⁸GESTAR-II University of Maryland Baltimore County, Baltimore, MD, USA. ⁹National Centre for Atmospheric Sciences, University of Leeds, Leeds, UK. ¹⁰School of Earth and Environment, University of Leeds, Leeds, UK. ¹¹Department of Meteorology and National Centre for Earth Observation, University of Reading, Berkshire, UK. ✉e-mail: y.chen.21@bham.ac.uk

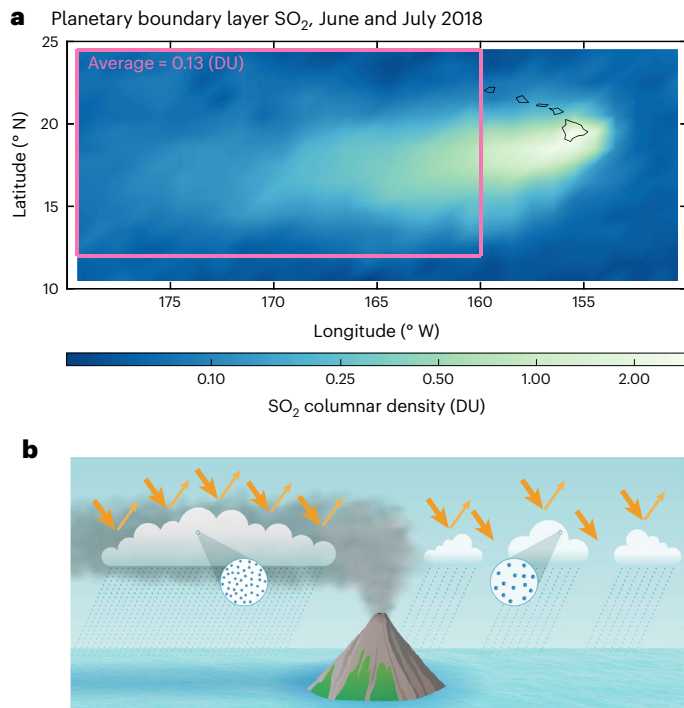


Fig. 1 | Kilauea volcanic plume. **a**, The SO₂ plumes observed by satellite in June and July 2018. The colour shows the SO₂ (Dobson unit, DU) plume in the planetary boundary layer observed by Ozone Mapping and Profiler Suite sensor on the Suomi-NPP satellite, launched in October 2011. Here we aggregate the daily level-two product of the boundary layer column SO₂ (horizontal resolution of about 50 km) to a two-month average. The studied region is marked by a pink box, where plume dispersal was sufficient and is also displaced from the Hawaii islands to avoid orographic effects. **b**, Conceptual picture of volcanic aerosol plume interacts with shallow convective marine clouds, leading to increase of cloud cover, precipitation and more reflected solar radiation back to space.

climate target^{5,6}. However, as this target is in peril⁴, proposals have emerged to help mitigate devastating climate impacts by conducting deliberate marine cloud brightening (MCB) to ‘buy some time’^{7,8} while the global economy is decarbonizing. At real-life regional scales, scientists are experimenting with MCB, aimed at saving the Great Barrier Reef from the seawater warming⁹. However, the efficacy and potential side effects¹⁰ of MCB are not well understood or well evaluated, due to an incomplete understanding of ACI.

The underlying principle of MCB is the ACI cooling effect, and the goal is to enhance the planetary albedo by seeding marine clouds with aerosols. The cooling effect of ACI originates from aerosols serving as cloud condensation nuclei, the seeds of cloud droplets. Higher aerosol loadings typically lead to more but smaller cloud droplets, resulting in enhanced cloud albedo and thus more sunlight reflection (Twomey effect)¹¹. Smaller cloud droplets could delay precipitation onset, leading to a longer cloud lifetime and hence larger cloud cover and water content (lifetime effect)¹². On the other hand, more but smaller cloud droplets could also enhance entrainment evaporation from dry free troposphere air, possibly leading to a decrease of cloud coverage and albedo (entrainment effect)¹³. The ACI climate impact is determined by the net effect of the above processes, which are poorly constrained or represented in global climate models (GCMs)^{11,14} resulting in large uncertainties in the magnitude and even the sign of the efficacy when evaluating MCB using multi-model ensembles¹⁰.

One reason for the slow progress in the development of realistic simulations of ACI in GCMs is the lack of observational constraints^{4,6}. Satellite observations of aerosol and clouds have been widely employed to study ACI using either small-scale natural experiments or large-scale climatological approaches. Whereas both are useful, they do not

provide sufficient constraints^{6,14,15}. Small-scale natural experiments, such as ship tracks and industrial plumes manifested as linear features of brighter clouds, are one prominent pathway to study ACI because confounding meteorological co-variability can generally be ruled out, for example, refs. 5,16, but ship tracks are subgrid scale compared with GCM resolutions. Large-scale climatological studies, for example, refs. 17,18, investigating spatio-temporal co-variability between aerosol and clouds, while more suitable for constraining large-scale GCMs¹⁹, are often contaminated by meteorological co-variability^{6,14}. Despite these respective limitations, aggregating a large observational ensemble of small-scale and large-scale satellite observations has resulted in convergence of ACI’s impacts on cloud microphysical properties^{5,18}: a larger cloud droplet number concentration (N_d) reduces cloud droplet effective radius (r_{eff}) and brightens clouds with negligible change in the ensemble-averaged cloud liquid water path (LWP). However, ACI’s impact on cloud macro-physical properties, such as cloud cover, is persistently disputed, with disagreement of several orders of magnitude between observations and models^{1,6,10,14}. This is because the large-scale nature of cloud macro-physical properties suggests that small-scale approaches struggle, for example, ship tracks cannot reveal cloud cover response over hundreds of kilometres scale. On the other hand, traditional climatological large-scale approaches also struggle due to confounding meteorological co-variability^{6,14,20}.

Early global modelling studies suggest that enhancing cloud albedo by doubling N_d could offset the warming from CO₂ doubling, but they also highlight the large uncertainty associated with cloud macro-physical properties²¹. Another modelling study estimated that degassing volcanoes increase tropical low-level clouds’ N_d by 16% in the present day, leading to a radiative effect (and associated cooling) of about -0.9 W m^{-2} in the tropics due to the Twomey effect²². However, the Twomey effect could only explain 20% of the increased reflection of sunlight observed by satellites for a degassing volcanic event from Hawaii²³. Previous studies^{23–25} suggest that cloud cover adjustment should play a crucial role in ACI cooling and hence MCB, but GCMs struggle to reproduce the observed strong relationship between aerosol and cloud cover^{14,17,26}. MCB could be significantly more effective if cloud cover were to increase strongly in response to aerosol injections^{10,27}, providing further motivation for this study.

Large-scale degassing volcanic eruptions offer ideal natural experiments to investigate the overall impacts of ACI on climate^{6,18,28} with implications for MCB. Our recent study developed a novel machine-learning approach to quantitatively disentangle aerosol fingerprints on clouds from the noise of meteorological co-variability and demonstrated its fidelity using a high-latitude degassing volcano in Iceland⁶. Building on this approach, we disentangle the aerosol fingerprints on tropical marine shallow convective clouds and further quantify volcanic aerosol’s radiative cooling as an analogue to MCB. We use four months of observations of volcanic eruptions in Hawaii (Fig. 1), each month with distinct meteorological conditions. These unique natural experiments in the tropics not only provide invaluable constraints for improving climate models but have practical implications for any potential MCB deployment. Whereas areas of stratocumulus frequently exceed 80% cloud cover²⁹, the cloud fraction in areas of tropical oceanic shallow convective clouds are frequently much less than 50%. Thus, any MCB-induced change in the cloud fraction in shallow convective areas could have a disproportionately large cooling impact. This was one motivation behind the Geoengineering Model Intercomparison Project-6 (GeoMIP6) whose solar radiation management simulations (G4sea-salt) modelled the effectiveness of injecting sea salt aerosols into the tropical marine boundary layer to offset a warming radiative forcing of 2 W m^{-2} (refs. 30–32).

Aerosol fingerprints on clouds

To quantify the aerosol fingerprint on clouds and hence evaluate the MCB, we build machine-learning surrogates of satellite observations

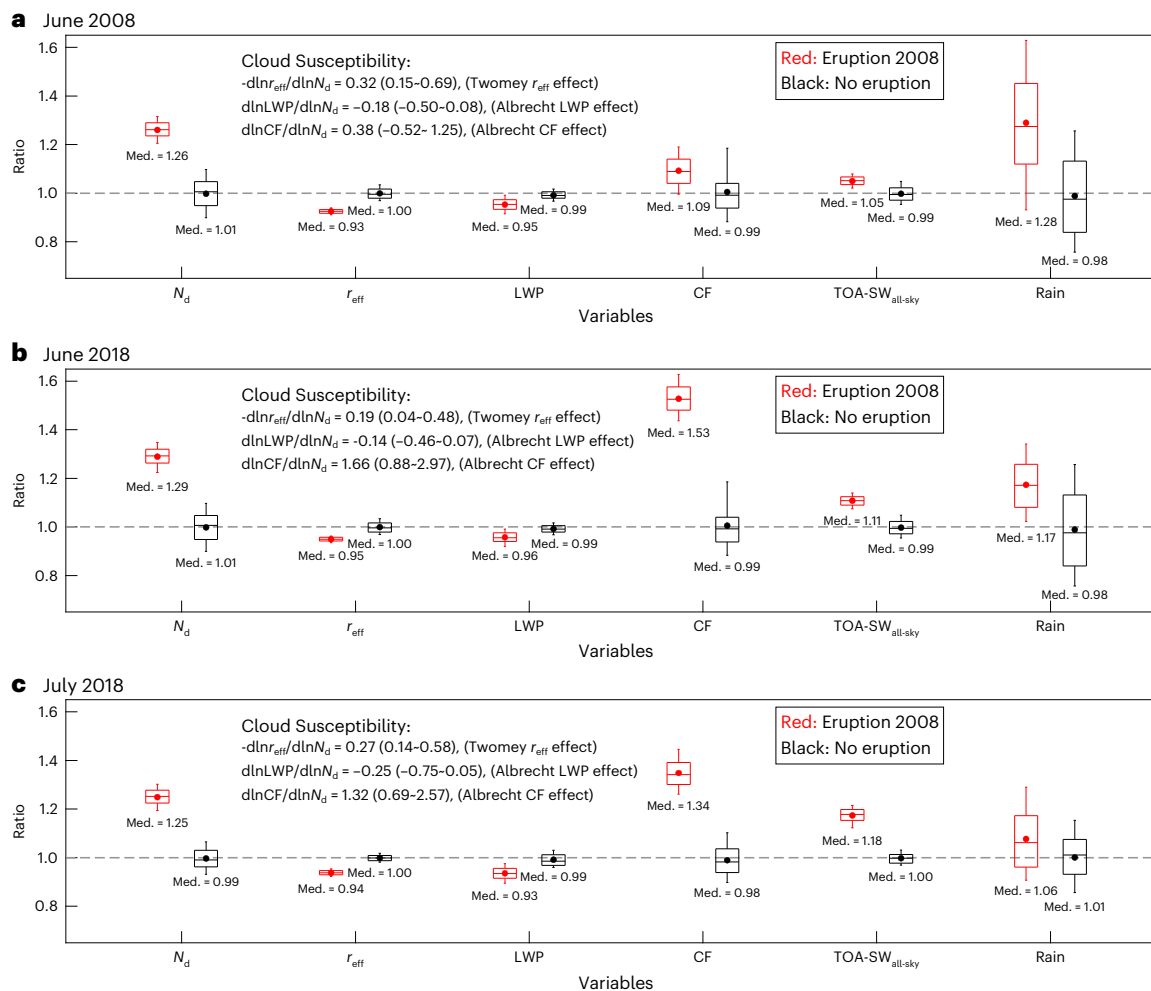


Fig. 2 | Aerosol fingerprints on clouds from natural experiments. a–c, June 2008 (a), June 2018 (b) and July 2018 (c). The aerosol-induced responses of clouds are shown in red, as ratios between observations and machine-learning surrogates; non-perturbed baselines of normal conditions are shown in black. The boxplots show 10th, 25th, median (Med.), 75th and 90th percentiles with the average indicated by a dot. Cloud droplet number concentration (N_d), cloud droplet effective radius (r_{eff}), cloud liquid water path (LWP) and cloud fraction (CF), top of atmosphere upward shortwave flux at all sky (TOA-SW_{all-sky}) and rainfall. The uncertainty is estimated by a bootstrapping Monte Carlo

method (Methods), with black boxes showing the validation of machine-learning surrogate against observations under normal conditions. The cloud susceptibilities are shown in black text, median (90% confidence interval). Area (in units of km^2) weighted averaging is used to calculate average cloud properties over the geographical region (the pink box in Fig. 1a), to estimate an unbiased large-scale response. All the ACI signals, that is, the differences between the red and black boxes, pass the Mann–Whitney–Wilcoxon test with significance $>95\%$ (P value < 0.05).

to diagnose counterfactual cloud properties and radiative fluxes for given meteorological conditions (Methods). Using this approach, we can reproduce clouds under ‘normal’ unperturbed conditions and compare to observations perturbed by volcanic eruptions. Surrogates are generated using 20 years of satellite observations of cloud properties, radiative energy fluxes, precipitation and co-located meteorological parameters and are well validated against observations using advanced statistical approaches (Fig. 2, Supplementary Section 1 and Extended Data Fig. 1; details also in Methods). Four months of degassing volcanic eruptions at Kilauea in Hawaii during June and July in 2008 and 2018 are investigated. The Hawaii-Kilauea volcanic outgassing events provide excellent natural experiments for assessing the effects of aerosol on clouds and climate due to the characteristics of the volcanic emissions and the pristine environment. These four experiments represent distinct meteorological conditions (Table 1 and Extended Data Fig. 2; also Methods), with a tropical cloud regime spectrum of mainly oceanic shallow convective clouds representing a very different but MCB-relevant case compared with our previous high-latitude study of the Holuhraun eruption in Iceland (Extended Data Fig. 3).

Almost all clouds in this studied region are likely to be precipitating, as suggested by $r_{\text{eff}} > 14 \mu\text{m}$ (Extended Data Fig. 2) and hence facilitating droplet growth by collision coalescence^{17,33}. The June 2008 case is a balance of different meteorological conditions, with a wide range of lower-tropospheric stability (LTS) and relative humidity (RH). LTS is calculated as the difference in the potential temperature between 700 hPa and the surface³⁴, and LTS $< 14 \text{ K}$ indicates strongly unstable conditions¹⁷. Here we analyse the RH at 850 hPa as being representative for the layer between 700 hPa and the ocean surface. July 2008 is a special case with distinct bimodality of very dry conditions in the south and humid air in the north of the studied region (Fig. 3a). The natural experiments in 2018 represent humid conditions with more stable conditions in June (nearly all LTS $> 14 \text{ K}$) than in July.

We find that the volcanic aerosol leads to a significant Twomey effect, with N_d increasing by 26–28% and r_{eff} decreasing by 5–7%, on average, over the region studied (Fig. 2 and Extended Data Figs. 4–7). This is consistent with many previous studies, for example, refs. 5,17,18,28,33,35, of the well-documented Twomey effect as an indicator of ACI, although these and other studies suggest that the

Table 1 | Description of meteorological conditions for each natural experiment case

Natural experiments	Description
2008-06	Wide range of RH and LTS, including very unstable conditions (LTS<14K)
2008-07	Special case: dry-stable conditions in the southern part and humid-unstable conditions in the northern part of the studied region
2018-06	Humid environment with dominantly RH>70%, very stable with nearly LTS>14K everywhere
2018-07	Very humid environment with dominantly RH>75%, medium stability

The meteorological details are analysed in Extended Data Fig. 2.

LWP adjustment is unclear overall, with both increases, decreases and no changes reported^{5,6,16,18,33,36,37}. Our observations indicate a statistically significant 4–6% decrease of the in-cloud LWP when aggregated over the region, independent of initial weather conditions. This is somewhat different to the conclusions from our study of the Holuhraun volcanic eruption⁶, where very different high-latitude meteorological conditions prevailed and LWP did not change. The Holuhraun eruption occurred in a region where about 40% of the clouds are precipitating, whereas the Kilauea eruption occurred in a tropical region dominated by shallow oceanic convective clouds (Extended Data Fig. 3), 90% of which are likely to be precipitating (indicated by $r_{\text{eff}} > 14 \mu\text{m}$ (ref. 17)). The decrease in LWP that we diagnose could be due to an increase of rainfall (Fig. 2), as clouds are still precipitating despite the reduction in r_{eff} and/or because of entrainment of dry air inducing cloud evaporation, as indicated by the dry southern part of the domain in July 2008 (Fig. 3a). The reduction of in-cloud LWP counteracts the brightening from the Twomey effect, a process known as ‘buffering’³⁸.

However, we find a strong increase in cloud cover (also known as cloud fraction, CF), due to the volcanic aerosol injection. This, in conjunction with the aerosol direct effect, enhances the shortwave cooling at the top of atmosphere (TOA). Increased aerosol leads to a direct radiative effect of -2 W m^{-2} in June 2008, -5 W m^{-2} in June 2018 and -4.2 W m^{-2} in July 2018. ACI adds extra radiative effect averaged over the region by about -2 W m^{-2} , -2.8 W m^{-2} and -10.5 W m^{-2} in June 2008, June 2018 and July 2018, respectively, despite there being only 10–16% cloudy skies. We estimate the relative contributions to ACI shortwave forcing using equation (1) (Methods) and find that the cooling radiative forcing from cloud cover enhancement contributes 65% in the balanced and more generalized conditions of June 2008 versus 84–87% in the humid conditions in 2018. Cooling forcing from the albedo enhancement by the Twomey effect amounts to 64% in June 2008 versus 25–34% in humid conditions. But warming forcing from LWP adjustment partially compensates cloud albedo cooling (-29% in June 2008; -9% to -21% in humid conditions). To show that this strong cooling forcing is indeed resulted from aerosol perturbation, we provide a similar analysis upwind on the volcanic plume. The results show weak or negligible ACI signals (and the associated radiative forcing) in the slightly polluted or non-polluted upwind region (Supplementary Section 1). Although June 2018 shows the strongest relative increase of cloud cover by +54% (Fig. 2b, $1.53 - 0.99 = 54\%$), July 2018 shows a stronger enhanced TOA shortwave reflection by +18%. This is possibly due to the different solar zenith angles and meteorology across these two months as the machine-learning approach is designed to remove meteorological co-variability within each individual month but not meteorological difference across different months. It could also be partly due to the uncertainty associated with anomalous high clouds in July 2018 in the southern part of the domain ($<15^\circ \text{N}$). By removing this southern part, similar aerosol fingerprints on clouds are found, indicating this uncertainty does not significantly impact the core findings of this study (Supplementary Section 2).

We find a high susceptibility of cloud cover to changes in N_d ($d\ln\text{CF} / d\ln N_d = 0.38$; Fig. 2a) for the more generalized case of June 2008 covering a wide range of meteorological conditions. This value is similar to our previous study of the Holuhraun natural experiment⁶, which also covers a wide range, yet different, meteorological conditions in the North Atlantic. Extremely high cloud cover susceptibility ($d\ln\text{CF} / d\ln N_d > 1.0$) is found in humid conditions (in 2018 and in the northern humid region in July 2008); $d\ln\text{CF} / d\ln N_d$ can reach up to 1.6 in humid and stable conditions (June 2018; Fig. 2), which favours higher cloud cover^{34,39}. This means that a 30% increase of N_d , the estimate of the averaged increase from pre-industrial to present-day conditions¹⁴, could potentially lead to a 10% relative increase in cloud cover overall (for example, Holuhraun⁶ and June 2008 cases with a mixture of meteorological conditions) and up to a 50% relative increase under humid and stable conditions (Fig. 4). Increasing N_d under humid and stable conditions can lead to strong TOA cooling; whereas contrastingly under dry conditions, it can suppress cloud cover increases (Fig. 3d) through more cloud top entrainment and cloud droplet evaporation.

Efficacy of marine cloud brightening

Recent research underlines the remarkable impacts of aerosols on clouds and climate change, and the fact that these strong impacts are potentially concealed when using traditional analysis approaches that suffer from biases associated with sampling, scale limitations and meteorological co-variability^{16,19,20,40}. In this study of Kilauea natural experiments, we overcome the challenges of sampling small-scale episodes and are able to quantify the significant aerosol fingerprints on clouds and climate forcing by investigating a large region ($2,500 \text{ km} \times 1,500 \text{ km}$) and by ruling out the noise of meteorological co-variability using a long-term observation-based machine-learning approach (Methods). The uncertainty in satellite retrievals over low latitudes is expected to be relatively small compared with higher latitudes due to smaller solar zenith angles^{41,42}, although some systematic underestimation in cloud cover has been reported for shallow convective clouds⁴³. In addition, random uncertainties in satellite retrievals are naturally cancelled out with averaging over a large region, and systematic uncertainties are minimized as well by comparing satellite observations against their machine-learning surrogates⁶.

Our findings suggest that MCB may be quite effective for alleviating climate warming, although it would probably manifest as an increase in cloud cover rather than cloud opacity, as the MCB terminology implies. This is in line with a recent cloud-resolving large-eddy simulation of MCB²⁵. Climate modelling studies suggest that offsetting the warming from CO_2 doubling by enhancing marine cloud albedos requires an increase in N_d by 200–300% (refs. 21,44). The stronger cooling from cloud cover adjustment than from the cloud albedo effect suggests that MCB could be more effective and achievable than the model previously suggested. Our results also suggest that the most practicable approach would be to seed clouds under humid and stable conditions (Fig. 4) where cloud cover might substantially expand; even if clouds are missed and seeding is into clear sky, the hygroscopic-swelled aerosol can also contribute a large cooling^{30,32,45}. This optimal approach is demonstrated by the June 2018 case where cloud cover increased by 54% and resulted in a strong TOA cooling. Seeding clouds under dry conditions could lead to reduction of cloud cover and warming, opposing the intention to increase reflected solar radiation to space. This best practice would be particularly effective in tropical oceans where incoming solar radiation is strong and background environment is clean (that is, clouds are more ‘pristine’).

While effective, MCB can only be seen as a ‘pain killer’, because it does not address the cause of warming from anthropogenic greenhouse gases. Our results illustrate the high potential risk of unforeseen large ‘side effects’ of MCB, owing to the large uncertainty due to a poor understanding of aerosol–cloud interactions. This new finding

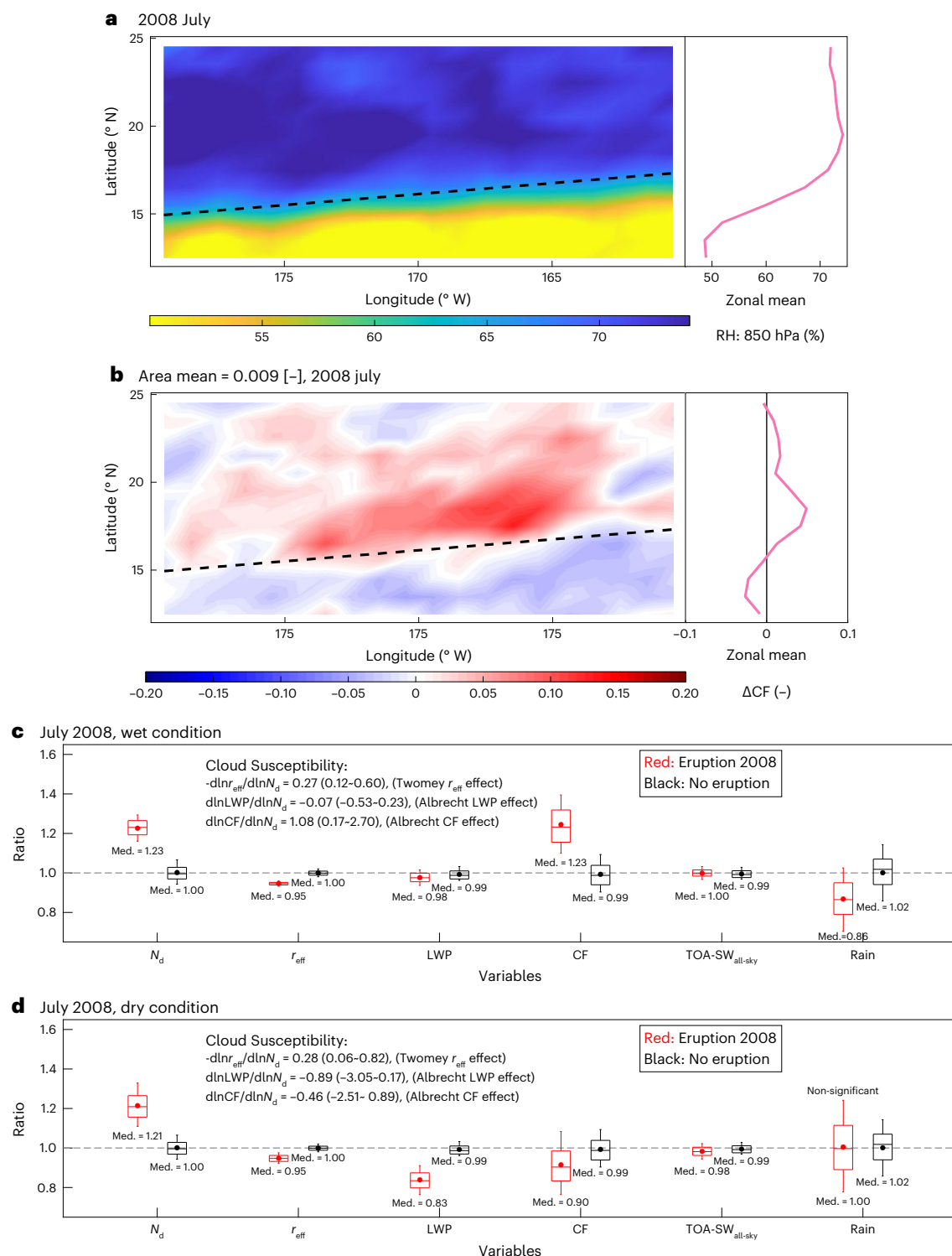


Fig. 3 | Aerosol fingerprints on clouds. Natural experiment of July 2008 with humid condition in the northern part and very dry conditions in the southern part. **a–d**, The distribution of RH at 850 hPa (**a**), the response of cloud fraction to aerosol perturbations (**b**), ACI manifestations for wet conditions (**c**) and ACI manifestations for dry conditions (**d**). The boxplots show 10th, 25th, median (Med.), 75th and 90th percentiles with the average indicated by a dot. Cloud

droplet number concentration (N_d), cloud droplet effective radius (r_{eff}), cloud liquid water path (LWP) and cloud fraction (CF), top of atmosphere upward shortwave flux at all sky (TOA-SW_{all-sky}) and rainfall. All the fingerprint signals pass the Mann–Whitney–Wilcoxon test with significance $>95\%$, unless marked as ‘non-significant’.

of a large-scale strong cloud cover response taking place in different climate and cloud regimes, as demonstrated by the high-latitude Holuhraun⁶ and tropical Kilauea eruption natural experiments, is, however, not replicated by state-of-the-art GCMs^{1,6,10,14,39}. It is paramount

that we close current gaps in ACI knowledge in a fundamental way not only to advance our understanding of Earth climate system and its hydrological cycle but also for a holistic evaluation of the benefits and risks of MCB.

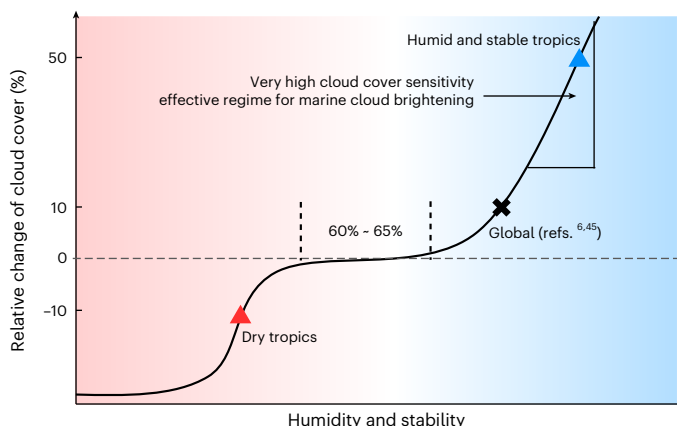


Fig. 4 | Conceptual model of cloud cover's response to aerosol perturbation.

The responses of cloud cover to 30% increase in N_d depend on meteorology conditions and cloud regimes. The Holuhraun study in ref. 6 represents a more generalized analogy for the global cloud regime spectrum, whereas this study represents a cloud regime spectrum for tropical marine clouds that could potentially be used for marine cloud brightening; they are all marked in the figure. The colour gradation from blue to red demonstrates the efficacy of MCB, with cooling in blue but warming in red. The effective meteorology regime for MCB is highlighted in blue.

Such a strong increase of large-scale cloud cover has remained undetected in many previous studies, for example, refs. 5,16,18,19,46, and has been intensely debated in several modelling and climatological studies^{17,24,25,28,47,48}. The current theoretical understanding suggests that cloud cover increases via inhibition of precipitation¹², whereas our new findings demonstrate that cloud cover can increase even as rainfall strengthens (Fig. 2). We propose the following hypothesis to explain this phenomenon. As more aerosols activate, N_d increases, leading to the Twomey effect. For stratocumulus clouds embedded in an aerosol-abundant regime, this can inhibit precipitation and hence increase cloud lifetime. In an aerosol-limited and convective regime, the Twomey effect reduces r_{eff} but not sufficiently to efficiently slow down collision coalescence, hence it is not effective in inhibiting rainfall. Instead, when the atmosphere is humid, an increase of aerosols not only prolongs the lifetime of precipitating clouds but could also facilitate cloud detrainment (as suggested by the decrease of LWP), which humidifies the area surrounding clouds and leads to horizontal expansion of the precipitating clouds to larger areas and more rainfall (Fig. 1b). Our case of tropical shallow convective clouds in a pristine marine environment²⁸, with $r_{\text{eff}} > 14 \mu\text{m}$ and N_d mostly in the range of $15\text{--}35 \text{ cm}^{-3}$ (Extended Data Fig. 1), is considered an aerosol-limited regime⁴⁹. The mechanism that we are proposing would mean that new particle formation plays an even more critical role in Earth climate system than previously thought, especially in aerosol-limited environments (such as pre-industrial) where new particle formation is a major source of cloud condensation nuclei and where cloud cover is highly susceptible to increases in aerosol⁵⁰. This mechanism needs to be tested by further research, ideally by large-eddy modelling of both the Holuhraun and Kilauea eruptions to reproduce the different ACI mechanisms prevailing in different meteorological and cloud regimes. A more detailed representation of subgrid-scale variability than diagnostic schemes currently used in most climate models^{51,52} could also serve as a plausible direction to improve ACI and hence predicted cloud feedbacks, which remains the largest source of uncertainty in climate projections for decades.

This study sheds additional light on the understanding of aerosol fingerprints on clouds, especially with regard to cloud cover response. This is critical for more reliable climate projections and underscores the urgent need to have a sound theoretical foundation and a holistic

assessment of any potential risks before implementing global warming mitigation strategies, such as MCB.

Online content

Any methods, additional references, Nature Portfolio reporting summaries, source data, extended data, supplementary information, acknowledgements, peer review information; details of author contributions and competing interests; and statements of data and code availability are available at <https://doi.org/10.1038/s41561-024-01427-z>.

References

1. IPCC Climate Change 2021: *The Physical Science Basis* (eds Masson-Delmotte, V. et al.) (Cambridge Univ. Press, 2021); <https://doi.org/10.1017/9781009157896>
2. Watson-Parris, D. & Smith, C. J. Large uncertainty in future warming due to aerosol forcing. *Nat. Clim. Change* <https://doi.org/10.1038/s41558-022-01516-0> (2022).
3. Bellouin, N. et al. Bounding global aerosol radiative forcing of climate change. *Rev. Geophys.* **58**, e2019RG000660 (2020).
4. Hansen, J. E. et al. Global warming in the pipeline. *Oxford Open Clim. Change* <https://doi.org/10.1093/oxfclm/kgad008> (2023).
5. Toll, V., Christensen, M., Quaas, J. & Bellouin, N. Weak average liquid–cloud–water response to anthropogenic aerosols. *Nature* **572**, 51–55 (2019).
6. Chen, Y. et al. Machine learning reveals climate forcing from aerosols is dominated by increased cloud cover. *Nat. Geosci.* <https://doi.org/10.1038/s41561-022-00991-6> (2022).
7. Latham, J. et al. Marine cloud brightening. *Philos. Trans. R. Soc. A* **370**, 4217–4262 (2012).
8. Connolly, P. J., McFiggans, G. B., Wood, R. & Tsiamis, A. Factors determining the most efficient spray distribution for marine cloud brightening. *Philos. Trans. R. Soc. A* **372**, 20140056 (2014).
9. Tollefson, J. Can artificially altered clouds save the Great Barrier Reef? *Nature* **596**, 476–478 (2021).
10. Stjern, C. W. et al. Response to marine cloud brightening in a multi-model ensemble. *Atmos. Chem. Phys.* **18**, 621–634 (2018).
11. Twomey, S. Pollution and the planetary albedo. *Atmos. Environ.* **8**, 1251–1256 (1974).
12. Albrecht, B. A. Aerosols, cloud microphysics, and fractional cloudiness. *Science* **245**, 1227–1230 (1989).
13. Ackerman, A. S., Kirkpatrick, M. P., Stevens, D. E. & Toon, O. B. The impact of humidity above stratiform clouds on indirect aerosol climate forcing. *Nature* **432**, 1014–1017 (2004).
14. Ghan, S. et al. Challenges in constraining anthropogenic aerosol effects on cloud radiative forcing using present-day spatiotemporal variability. *Proc. Natl. Acad. Sci. USA* **113**, 5804–5811 (2016).
15. Seinfeld, J. H. et al. Improving our fundamental understanding of the role of aerosol–cloud interactions in the climate system. *Proc. Natl. Acad. Sci. USA* **113**, 5781–5790 (2016).
16. Manshausen, P., Watson-Parris, D., Christensen, M. W., Jalkanen, J.-P. & Stier, P. Invisible ship tracks show large cloud sensitivity to aerosol. *Nature* **610**, 101–106 (2022).
17. Rosenfeld, D. et al. Aerosol-driven droplet concentrations dominate coverage and water of oceanic low-level clouds. *Science* **363**, eaav0566 (2019).
18. Malavelle, F. F. et al. Strong constraints on aerosol–cloud interactions from volcanic eruptions. *Nature* **546**, 485–491 (2017).
19. Glassmeier, F. et al. Aerosol–cloud–climate cooling overestimated by ship-track data. *Science* **371**, 485–489 (2021).
20. Quaas, J. et al. Constraining the Twomey effect from satellite observations: issues and perspectives. *Atmos. Chem. Phys.* **20**, 15079–15099 (2020).

21. Latham, J. et al. Global temperature stabilization via controlled albedo enhancement of low-level maritime clouds. *Philos. Trans. R. Soc. A* **366**, 3969–3987 (2008).

22. Schmidt, A. et al. Importance of tropospheric volcanic aerosol for indirect radiative forcing of climate. *Atmos. Chem. Phys.* **12**, 7321–7339 (2012).

23. Yuan, T., Remer, L. A. & Yu, H. Microphysical, macrophysical and radiative signatures of volcanic aerosols in trade wind cumulus observed by the A-Train. *Atmos. Chem. Phys.* **11**, 7119–7132 (2011).

24. Goren, T. & Rosenfeld, D. Decomposing aerosol cloud radiative effects into cloud cover, liquid water path and Twomey components in marine stratocumulus. *Atmos. Res.* **138**, 378–393 (2014).

25. Prabhakaran, P., Hoffmann, F. & Feingold, G. Evaluation of pulse aerosol forcing on marine stratocumulus clouds in the context of marine cloud brightening. *J. Atmos. Sci.* **80**, 1585–1604 (2023).

26. Quaas, J., Stevens, B., Stier, P. & Lohmann, U. Interpreting the cloud cover–aerosol optical depth relationship found in satellite data using a general circulation model. *Atmos. Chem. Phys.* **10**, 6129–6135 (2010).

27. Slingo, A. Sensitivity of the Earth’s radiation budget to changes in low clouds. *Nature* **343**, 49–51 (1990).

28. Breen, K. H., Barahona, D., Yuan, T., Bian, H. & James, S. C. Effect of volcanic emissions on clouds during the 2008 and 2018 Kilauea degassing events. *Atmos. Chem. Phys.* **21**, 7749–7771 (2021).

29. Muhlbauer, A., McCoy, I. L. & Wood, R. Climatology of stratocumulus cloud morphologies: microphysical properties and radiative effects. *Atmos. Chem. Phys.* **14**, 6695–6716 (2014).

30. Kravitz, B. et al. Sea spray geoengineering experiments in the geoengineering model intercomparison project (GeoMIP): experimental design and preliminary results. *J. Geophys. Res.: Atmos.* **118**, 11,175–11,186 (2013).

31. Kravitz, B. et al. The Geoengineering Model Intercomparison Project Phase 6 (GeoMIP6): simulation design and preliminary results. *Geosci. Model Dev.* **8**, 3379–3392 (2015).

32. Ahlm, L. et al. Marine cloud brightening—as effective without clouds. *Atmos. Chem. Phys.* **17**, 13071–13087 (2017).

33. Toll, V., Christensen, M., Gassó, S. & Bellouin, N. Volcano and ship tracks indicate excessive aerosol-induced cloud water increases in a climate model. *Geophys. Res. Lett.* **44**, 12,492–412,500 (2017).

34. Wood, R. & Bretherton, C. S. On the relationship between stratiform low cloud cover and lower-tropospheric stability. *J. Clim.* **19**, 6425–6432 (2006).

35. Christensen, M. W., Jones, W. K. & Stier, P. Aerosols enhance cloud lifetime and brightness along the stratus-to-cumulus transition. *Proc. Natl Acad. Sci. USA* **117**, 17591–17598 (2020).

36. Gryspeerd, E. et al. Constraining the aerosol influence on cloud liquid water path. *Atmos. Chem. Phys.* **19**, 5331–5347 (2019).

37. Yuan, T. et al. Observational evidence of strong forcing from aerosol effect on low cloud coverage. *Sci. Adv.* **9**, eadh7716 (2023).

38. Stevens, B. & Feingold, G. Untangling aerosol effects on clouds and precipitation in a buffered system. *Nature* **461**, 607–613 (2009).

39. Quaas, J. Evaluating the ‘critical relative humidity’ as a measure of subgrid-scale variability of humidity in general circulation model cloud cover parameterizations using satellite data. *J. Geophys. Res.* <https://doi.org/10.1029/2012JD017495> (2012).

40. Arola, A. et al. Aerosol effects on clouds are concealed by natural cloud heterogeneity and satellite retrieval errors. *Nat. Commun.* **13**, 7357 (2022).

41. Grosvenor, D. P. et al. Remote sensing of droplet number concentration in warm clouds: a review of the current state of knowledge and perspectives. *Rev. Geophys.* **56**, 409–453 (2018).

42. Grosvenor, D. P. & Wood, R. The effect of solar zenith angle on MODIS cloud optical and microphysical retrievals within marine liquid water clouds. *Atmos. Chem. Phys.* **14**, 7291–7321 (2014).

43. Mieslinger, T. et al. Optically thin clouds in the trades. *Atmos. Chem. Phys.* **22**, 6879–6898 (2022).

44. Wood, R. Assessing the potential efficacy of marine cloud brightening for cooling Earth using a simple heuristic model. *Atmos. Chem. Phys.* **21**, 14507–14533 (2021).

45. Chen, Y. et al. Ammonium chloride associated aerosol liquid water enhances haze in Delhi, India. *Environ. Sci. Technol.* **56**, 7163–7173 (2022).

46. Yuan, T. et al. Global reduction in ship-tracks from sulfur regulations for shipping fuel. *Sci. Adv.* **8**, eabn7988 (2022).

47. Gryspeerd, E., Quaas, J. & Bellouin, N. Constraining the aerosol influence on cloud fraction. *J. Geophys. Res.* **121**, 3566–3583 (2016).

48. Quaas, J. et al. Robust evidence for reversal in the aerosol effective climate forcing trend. *Atmos. Chem. Phys.* **22**, 12221–12239 (2022).

49. Misumi, R. et al. Classification of aerosol–cloud interaction regimes over Tokyo. *Atmos. Res.* **272**, 106150 (2022).

50. Kirkby, J. et al. Ion-induced nucleation of pure biogenic particles. *Nature* **533**, 521–526 (2016).

51. Muench, S. & Lohmann, U. Developing a cloud scheme with prognostic cloud fraction and two moment microphysics for ECHAM-HAM. *J. Adv. Model. Earth Syst.* **12**, e2019MS001824 (2020).

52. Tompkins, A. M. A prognostic parameterization for the subgrid-scale variability of water vapor and clouds in large-scale models and its use to diagnose cloud cover. *J. Atmos. Sci.* **59**, 1917–1942 (2002).

Publisher’s note Springer Nature remains neutral with regard to jurisdictional claims in published maps and institutional affiliations.

Open Access This article is licensed under a Creative Commons Attribution 4.0 International License, which permits use, sharing, adaptation, distribution and reproduction in any medium or format, as long as you give appropriate credit to the original author(s) and the source, provide a link to the Creative Commons licence, and indicate if changes were made. The images or other third party material in this article are included in the article’s Creative Commons licence, unless indicated otherwise in a credit line to the material. If material is not included in the article’s Creative Commons licence and your intended use is not permitted by statutory regulation or exceeds the permitted use, you will need to obtain permission directly from the copyright holder. To view a copy of this licence, visit <http://creativecommons.org/licenses/by/4.0/>.

© The Author(s) 2024

Methods

Natural experiment of Kilauea volcano on Hawaii

Kilauea is a volcano on the island of Hawaii (19° 34' N, 155° 30' W), situated in the middle of the North Pacific Ocean thousands of kilometres away from major anthropogenic emission sources. The marine environment surrounding Kilauea is close to pristine^{23,28} with concentrations of cloud condensation nuclei thought to be close to those of pre-industrial conditions in summertime⁵³. Therefore, the degassing eruptions of Kilauea serve as excellent natural experiments to investigate how clouds respond to aerosol perturbations (that is, aerosol–cloud interactions, ACI).

Kilauea was strongly active in June–August 2008 and May–July 2018²⁸, with SO₂ emission peaks over 10 kiloton per day in 2008⁵⁴ and over 100 kiloton per day in 2018⁵⁵. The volcanic SO₂ plumes (Fig. 1) and subsequently oxidation-formed particulate sulfate, which was efficiently dispersed over the downwind marine region as far as 6,000 km (ref. 23). The plumes reached up to 1,200–2,500 m height in 2008, and about 2 to 8 km height in 2018⁵⁵. Here we chose the months of June and July, which are common to both volcanic periods in 2008 and 2018 and allow us to distinguish aerosol fingerprints on shallow convective marine clouds in the tropics under different meteorological conditions. The natural experiment study focused on a downstream region (12° N–25° N, 160° W–180° W) strongly impacted by volcanic plumes (Fig. 1 and also Fig. 2 in ref. 28).

Normal conditions of clouds and precipitation from machine learning

Following our recent study⁶, machine learning (ML, details given later) is adopted to train a surrogate for the Moderate Resolution Imaging Spectroradiometer (MODIS). This ML surrogate is designed to diagnose cloud properties, which are unperturbed by volcanic aerosols. The performance of the ML surrogate in reproducing satellite observations under normal conditions (without the perturbation of volcanic aerosol) is demonstrated using the ‘leave-one-year-out’ cross validation⁵⁶. Here one normal year is held for validation; the ML is trained based on the datasets of the other normal years, and the evaluation is performed once for each normal year in 2001–2020 (left panels of Extended Data Fig. 1). We further estimate the uncertainty of the ML surrogate using a more statistically robust bootstrapping Monte Carlo method. This method selects two out of 18 normal years (2001–2020 excluding 2008 and 2018) as the hold years for validation in a bootstrapping way (uniform sampling with replacement) and trains ML based on the remaining normal years. This greatly enlarges the diversity of the sample pool, with 324 (18 × 18) different sample variants in total and therefore improves the robustness of the statistical analysis. We repeated this bootstrapping select-validation process for each ML surrogate for 648 times (twice the number of the total variants), to ensure the pool is efficiently sampled. The bootstrapping validation of ML surrogates are shown in the black boxplots in Figs. 2 and 3c,d. The ratios between ML surrogate (without aerosol perturbation) and observations in volcanic years (2008 or 2018, with aerosol perturbation) are shown in the red boxplots of Figs. 2 and 3c,d. These red boxplots show the variability of the aerosol fingerprints on clouds. The significance of the statistical difference of cloud properties and precipitation between the perturbed and unperturbed conditions is tested by both the one-tail and two-tail Wilcoxon–Mann–Whitney test with *P* values < 0.05 (significance > 95%).

A 100-trees random forest algorithm is adopted to train the ML surrogate. Random forest is chosen because of its great capability to avoid overfitting and handle high-dimensional feature spaces with a relatively small sample size. Following our recent study⁶, each tree, with a regression mode and minimal leaf size value of seven, samples 60% of the training data with replacement. ML surrogate is trained based on 114 meteorological parameters (Supplementary Table 1) from the surface up to the 550-hPa level under which virtually all low-level liquid clouds occur. The training of the ML surrogate is performed for

June and July separately and is supervised by MODIS observations of cloud properties (cloud droplet number concentration: N_d ; droplet effective radius: r_{eff} ; cloud liquid water path: LWP and cloud fraction: CF) under normal conditions during 2001–2020 by excluding the volcanic years 2008 and 2018. The ML surrogate is therefore able to predict unperturbed cloud conditions and enables like-with-like comparisons against volcanic-perturbed clouds observed by MODIS in 2008 and 2018. This approach has been demonstrated to work excellently in discerning the large-scale aerosol fingerprint on clouds from the noise of meteorology co-variability⁶. To distinguish aerosol fingerprint on precipitation, this ML surrogate approach is also applied to the Global Precipitation Climatology Project (GPCP) dataset⁵⁷.

The ERA5 meteorological reanalysis from the European Centre for Medium-Range Weather Forecasts (ECMWF) is used to provide the best estimate of the atmospheric state⁵⁸ for ML surrogate training. We take ERA5 monthly averages of meteorological conditions at 0.25° × 0.25° horizontal resolution from the surface up to 550 hPa at 50-hPa intervals and aggregate them to MODIS and GPCP grid cells at the time of *Aqua* and *Terra* daytime overpasses. The ERA5 meteorology corresponding to *Aqua* and *Terra* overpassing time is used in this study. The top-ten most important meteorological variables for predicting CF in 2008 and 2018 are mostly lying within the variation range of the training dataset, indicating reliable ML training⁶. The only exception is the unprecedented dry condition (850 hPa RH < 50%) in the southern part of the studied region in July 2008, which lies outside the range of the training dataset. However, this exception is not expected to have a large influence on our cloud analysis, because the fraction of outliers is only about 10% of the total data points in July 2008. In addition, the extrapolation for these very dry conditions is performed in a regime where the cloud response has flattened out (Extended Data Fig. 8).

MODIS provides continuous satellite observations of clouds in June and July during 2003–2020 for *Aqua* and 2001–2020 for *Terra*. We use the latest MODIS Collection 6.1 Level-3 products, which has rectified retrieval biases in the previous Collection 5 and shows excellent consistency between *Aqua* and *Terra*¹⁸. The MODIS Level-3 monthly product is aggregated from Level-2 products with 1-km nadir resolution and provides monthly mean values of cloud optical thickness, cloud phase, r_{eff} , LWP and CF. The ‘cloud optical property CF’ for liquid clouds⁵⁹ is used because it is based on the pixel population with successful retrieval of cloud optical properties and is consistent with the other microphysical retrievals used in this study. Following refs. 60,61, we derived N_d from daily Level-3 products of r_{eff} and cloud optical thickness and then aggregated the data to monthly mean values. The uncertainty in derived N_d is about 50% in general when averaging across a 1° × 1° grid cell⁴¹. This uncertainty is expected to be much smaller in this study, because of (1) lower uncertainty in the tropics compared with mid-latitudes⁴¹, (2) lower uncertainty in precipitating clouds⁴⁰ (>90% in this study) and also (3) extensive averaging over a 2,500 km × 1,500 km geographical region, which greatly suppresses random errors. Monthly products are adopted in this study to investigate the aerosol fingerprints on clouds and radiative forcing on a climate-relevant timescale. This is in line with many previous studies, which also used monthly or seasonal average products to investigate ACI^{6,18,23,28,62}. Although monthly averages can potentially have several different realizations owing to variability in individual days^{63–66}, which could lead to uncertainty in monthly analysis and is out of the scope of this study, the trained ML surrogate is able to reasonably reproduce the monthly averaged conditions of cloud properties (Fig. 2 and Supplementary Section 1) and therefore is suitable for investigating ACI signals on a climate-relevant timescale.

GPCP combines datasets from rain gauge stations, sounding observations and various satellites to provide the best estimate of precipitation on a global scale⁵⁷. The GPCP monthly rainfall with a 2.5° × 2.5° horizontal resolution in June and July 2001–2020 (excluding

2008 and 2018) is used to supervise the ML training of the GPCP surrogate to represent rainfall under unperturbed normal conditions.

Radiative effect

We further use the above mentioned ML approach to train a surrogate to represent the unperturbed top of the atmosphere (TOA) reflected shortwave flux, which is observed by the Clouds and the Earth's Radiant Energy System (CERES) on board the Terra and Aqua satellites⁶⁷. This enables us to quantify the volcanic aerosol impact on the radiative cooling. Following the above-explained bootstrapping approach, the ML surrogate of CERES is validated and the change in TOA reflected shortwave flux is quantified. This change includes the aerosol direct effect (or aerosol radiation interaction) in the clear sky and ACI effects in cloudy skies.

The radiative effect (associated with a cooling) for aerosol direct effect is estimated to be -2 W m^{-2} in June 2008, -5 W m^{-2} in June 2018 and -4.2 W m^{-2} in July 2018, based on the MODIS observations of aerosol optical depth (AOD) anomaly (0.2 in 2008, 0.27 in June 2018 and 0.28 in July 2018), cloud fraction and forcing efficiency⁶⁸. This estimate method and results are in line with ref. 23.

For ACI effects over cloudy skies, we estimate the contributions from the Twomey effect, LWP and CF adjustments to ACI-induced radiative cooling using the susceptibilities of cloud properties to aerosol-induced changes in N_d . The ACI-induced total radiative cooling can be described as equation (1)^{3,5,69}, which is a modified version of equation (3) in ref. 6. The relative contributions from the Twomey effect, LWP adjustment and cloud cover adjustment are described in equation (1) from left to right by the three terms in the square bracket.

$$\begin{aligned} \frac{dSW_{TOA}}{d \ln \text{Aerosol}} &= \frac{dSW_{TOA}}{d \ln \text{Aerosol}}|_{\text{albedo}} + \frac{dSW_{TOA}}{d \ln \text{Aerosol}}|_{\text{CF}} \\ &\approx -SW_{TOA} \times \frac{d \ln N_d}{d \ln \text{Aerosol}} \times \text{CF} \times \left[\frac{1}{3} A_{\text{cld}}(1 - A_{\text{cld}}) \right. \\ &\quad \left. + A_{\text{cld}}(1 - A_{\text{cld}}) \times \frac{5}{6} \frac{d \ln \text{LWP}}{d \ln N_d} + (A_{\text{cld}} - A_{\text{cs}}) \frac{d \ln \text{CF}}{d \ln N_d} \right] \end{aligned} \quad (1)$$

$$A_{\text{cld}} \approx \frac{0.15 \times \text{COD}}{2 + 0.15 \times \text{COD}} \quad (2)$$

where SW_{TOA} is the net shortwave solar radiation at the top of the atmosphere, dSW_{TOA} is the change of net shortwave solar radiation at the top of atmosphere (that is, instantaneous shortwave radiative forcing). A_{cld} is the shortwave cloud albedo for liquid clouds, which can be estimated from cloud optical depth (COD, observed by MODIS) using equation (2) assuming a solar zenith angle close to zero and an asymmetry factor of 0.85⁷⁰. The A_{cld} average over the studied period and region is about 0.35. A_{cs} is shortwave broadband ocean surface albedo under clear-sky conditions. A_{cs} under pristine conditions has an average value of 0.06 for the studied region⁷¹. We estimate an effective A_{cs} for the aerosol polluted ocean, using AOD anomaly and a state-of-the-art radiative transfer model (SOCRATES), which is also used in the UK Met Office climate models⁷². The effective A_{cs} is estimated by assuming sulfate aerosol with specific extinction of $4.8 \text{ m}^2 \text{ g}^{-1}$, asymmetry factor of 0.7 (at 670 nm, a wavelength that is reasonably representative of broadband fluxes⁷³), with a mono-modal log-normal distribution, and a mode radius of 0.05 μm and a standard deviation of 2⁷⁴. The estimated effective A_{cs} with AOD accounted is 0.2 in 2018 and 0.15 in 2008, in line with ref. 23.

Data availability

The Level-3 C6.1 MODIS cloud and aerosol observations from Aqua (MYD08_M3, https://doi.org/10.5067/MODIS/MYD08_M3.061) and Terra (MOD08_M3, https://doi.org/10.5067/MODIS/MOD08_M3.061) used in this study are available at the Atmosphere Archive and Distribution System Distributed Active Archive Center of National Aeronautics and Space Administration (LAADS-DAAC, NASA), <https://ladsweb.modaps.eosdis.nasa.gov>. Suomi-NPP

Ozone Mapping and Profiler Suite SO₂ v2.0 data⁷⁵ are available from NASA Suomi web database: snpp-omps.gesdisc.eosdis.nasa.gov. ERA5 datasets^{76,77} are available from the European Centre for Medium-range Weather Forecast (ECMWF) archive, <https://cds.climate.copernicus.eu>. GPCP v2.3 precipitation data^{78,79} are available from NCAR, <https://climatedataguide.ucar.edu/climate-data/gpcp-monthly-global-precipitation-climatology-project>. The Level-3 CERES EBAF Ed4.1 dataset⁶⁷ is available from the NASA CERES project website (<https://ceres.larc.nasa.gov/data/>). All data needed to evaluate the results in this study are present in the main text and the Supplementary Information.

Code availability

Code is available from the corresponding author on reasonable request.

References

53. Hamilton, D. S. et al. Occurrence of pristine aerosol environments on a polluted planet. *Proc. Natl. Acad. Sci. USA* **111**, 18466–18471 (2014).
54. Elias, T., Kern, C., Horton, K. A., Sutton, A. J. & Garbeil, H. Measuring SO₂ emission rates at Kilauea volcano, Hawaii, using an array of upward-looking UV spectrometers, 2014–2017. *Front. Earth Sci.* <https://doi.org/10.3389/feart.2018.00214> (2018).
55. Neal, C. A. et al. The 2018 rift eruption and summit collapse of Kilauea Volcano. *Science* **363**, 367–374 (2019).
56. Bastos, L. S. & O'Hagan, A. Diagnostics for gaussian process emulators. *Technometrics* **51**, 425–438 (2009).
57. Huffman, G. J. et al. The Global Precipitation Climatology Project (GPCP) combined precipitation dataset. *Bull. Am. Meteorol. Soc.* **78**, 5–20 (1997).
58. Hersbach, H. et al. The ERA5 global reanalysis. *Q. J. R. Meteorol. Soc.* **146**, 1999–2049 (2020).
59. Hubanks, P., Platnick, A. S., King, M. & Ridgway, B. MODIS Atmosphere L3 Gridded Product Algorithm Theoretical Basis Document (ATBD) and Users Guide (NASA, 2019); https://icdc.cen.uni-hamburg.de/fileadmin/user_upload/icdc_Dokumente/MODIS/MODIS_Collection6_AtmosphereL3_GriddedProduct_ATBDandUsersGuide_v4.1_Sep22_2015.pdf
60. Quaas, J., Boucher, O. & Lohmann, U. Constraining the total aerosol indirect effect in the LMDZ and ECHAM4 GCMs using MODIS satellite data. *Atmos. Chem. Phys.* **6**, 947–955 (2006).
61. Quaas, J., Boucher, O., Bellouin, N. & Kinne, S. Satellite-based estimate of the direct and indirect aerosol climate forcing. *J. Geophys. Res.* <https://doi.org/10.1029/2007JD008962> (2008).
62. McCoy, D. T. & Hartmann, D. L. Observations of a substantial cloud-aerosol indirect effect during the 2014–2015 Bárðarbunga-Veiðivötn fissure eruption in Iceland. *Geophys. Res. Lett.* **42**, 10,409–10,414 (2015).
63. Bony, S. et al. Observed modulation of the tropical radiation budget by deep convective organization and lower-tropospheric stability. *AGU Adv.* **1**, e2019AV000155 (2020).
64. Rasp, S., Schulz, H., Bony, S. & Stevens, B. Combining crowdsourcing and deep learning to explore the mesoscale organization of shallow convection. *Bull. Am. Meteorol. Soc.* **101**, E1980–E1995 (2020).
65. Rasp, S. et al. WeatherBench: a benchmark data set for data-driven weather forecasting. *J. Adv. Model. Earth Syst.* **12**, e2020MS002203 (2020).
66. Cho, N., Tan, J. & Oreopoulos, L. Classifying planetary cloudiness with an updated set of MODIS cloud regimes. *J. Appl. Meteorol. Climatol.* **60**, 981–997 (2021).
67. Loeb, N. G. et al. Clouds and the Earth's Radiant Energy System (CERES) energy balanced and filled (EBAF) top-of-atmosphere (TOA) edition-4.0 data product. *J. Clim.* **31**, 895–918 (2018).

68. Remer, L. A. & Kaufman, Y. J. Aerosol direct radiative effect at the top of the atmosphere over cloud free ocean derived from four years of MODIS data. *Atmos. Chem. Phys.* **6**, 237–253 (2006).
69. Ackerman, A. S. et al. Effects of aerosols on cloud albedo: evaluation of Twomey's parameterization of cloud susceptibility using measurements of ship tracks. *J. Atmos. Sci.* **57**, 2684–2695 (2000).
70. Feingold, G. et al. Analysis of albedo versus cloud fraction relationships in liquid water clouds using heuristic models and large eddy simulation. *J. Geophys. Res.* **122**, 7086–7102 (2017).
71. Jin, Z., Charlock, T. P., Smith Jr., W. L. & Rutledge, K. A parameterization of ocean surface albedo. *Geophys. Res. Lett.* <https://doi.org/10.1029/2004GL021180> (2004).
72. Manners, J., Edwards, J. M., Hill, P. & Thelen, J. C. *SOCRATES Technical Guide: Suite Of Community RAdiative Transfer Codes Based on Edwards and Slingo* (Met Office, 2017).
73. Haywood, J. M. & Shine, K. P. The effect of anthropogenic sulfate and soot aerosol on the clear sky planetary radiation budget. *Geophys. Res. Lett.* **22**, 603–606 (1995).
74. *A Preliminary Cloudless Standard Atmosphere for Radiation Computation* Report No. WCP-112, WMO/TD-No. 24 (WMO, 1986).
75. Li, C., Krotkov, N. A., Leonard, P. & Joiner, J. OMPS/NPP PCA SO₂ Total Column 1-Orbit L2 Swath 50×50 km V2 (GES DISC, 2020); <https://doi.org/10.5067/MEASURES/SO2/DATA205>
76. Hersbach, H. et al. ERA5 hourly data on single levels from 1940 to present. C3S CDS <https://doi.org/10.24381/cds.adbb2d47> (2023).
77. Hersbach, H. et al. ERA5 hourly data on pressure levels from 1940 to present. C3S CDS <https://doi.org/10.24381/cds.bd0915c6> (2023).
78. Adler, R. F. et al. The Global Precipitation Climatology Project (GPCP) monthly analysis (new version 2.3) and a review of 2017 global precipitation. *Atmosphere* **9**, 138 (2018).
79. Adler, R. et al. Global Precipitation Climatology Project (GPCP) Climate Data Record (CDR), version 2.3 (monthly). *Natl Cent. Environ. Inf.* <https://doi.org/10.7289/V56971M6> (2016).

Acknowledgements

Y.C. is supported by the start-up fund from the University of Birmingham. A.P., J.H., D.G.P., D.G. and P.F. are supported by the UKRI Natural Environment Research Council (NERC) funded ADVANCE project (NE/T006897/1). Y.W. thanks the University of Edinburgh start-up fund, ETH Zurich Foundation (ETH fellowship project: 2021-HS-332) and P. Sarasin. J.H., G.J. and F.M. were also partly funded under funding provided by the EU's Horizon 2020 research and innovation programme under the CONSTRAIN grant agreement 820829. J.H., P.F., G.J. and F.M. are supported by the Joint UK BEIS/Defra Met Office Hadley Centre Climate Programme (GA01101). J.H. is also supported by the SilverLining Safe Climate Research Initiative. D.G. is funded by the National Centre for Atmospheric Science (NCAS),

one of the UK NERC's research centres. N.C. and L.O. are funded by USA NASA programmes. The machine-learning training is performed using the 'Statistics and Machine Learning Toolbox' in MATLAB (version R2022a, MathWorks). The data storage and processing are performed on high performance computers Stratus, Nimbus and Cumulus, which are supported by the University of Exeter. The findings and opinions expressed in this study do not necessarily represent the views of the funders. For the purpose of open access, a CC BY public copyright license is applied to any Author Accepted Manuscript arising from this submission. We would like to thank S. Platnick (NASA) for useful discussion in interpreting MODIS observations and uncertainty and C. Jackson (University of Birmingham) for her contribution to the conceptual figure (Fig. 1b).

Author contributions

Conceptualization: Y.C., Y.W., J.H., U.L. Methodology: Y.W., Y.C., J.H. Investigation: Y.C., J.H., Y.W., U.L., F.M., G.J., A.P., D.G.P., L.O., N.C., R.A. Visualization: Y.C., Y.W. Funding acquisition: J.H., Y.W., Y.C. Writing—original draft: Y.C., Y.W., J.H. Writing—review and editing: Y.C., Y.W., J.H., U.L., D.G.P., D.G., G.J., O.L., R.A. with input from all co-authors.

Ethics and inclusion statement

The authors declare that all researchers contributed to this study and fulfil the authorship criteria as stated by *Nature* are included as co-authors. This study does not result in any health, safety, security, stigmatization, incrimination, discrimination or personal risk to researchers.

Competing interests

The authors declare no competing interests.

Additional information

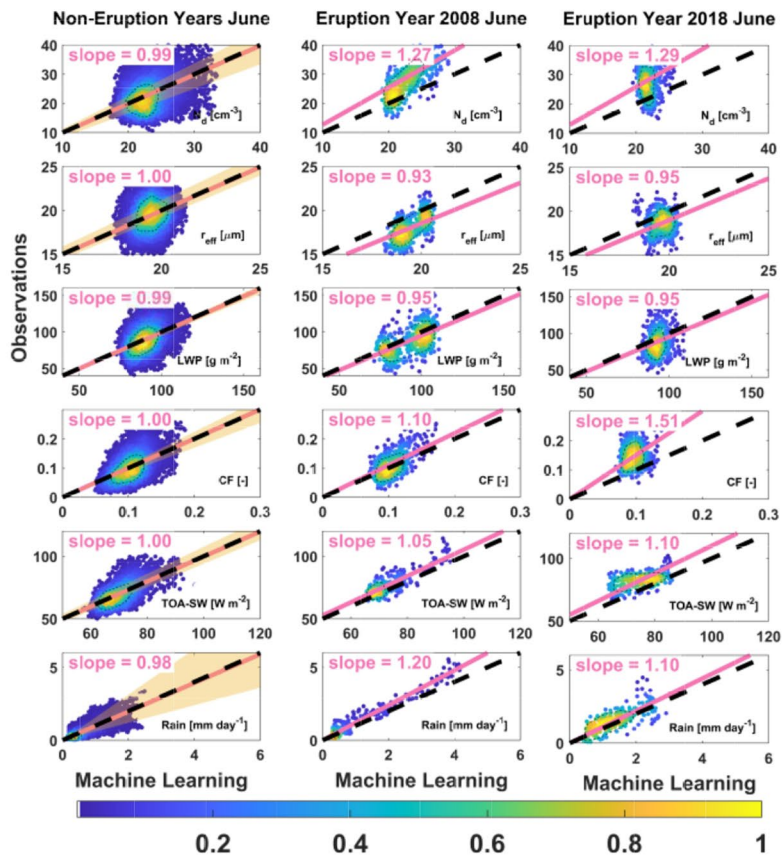
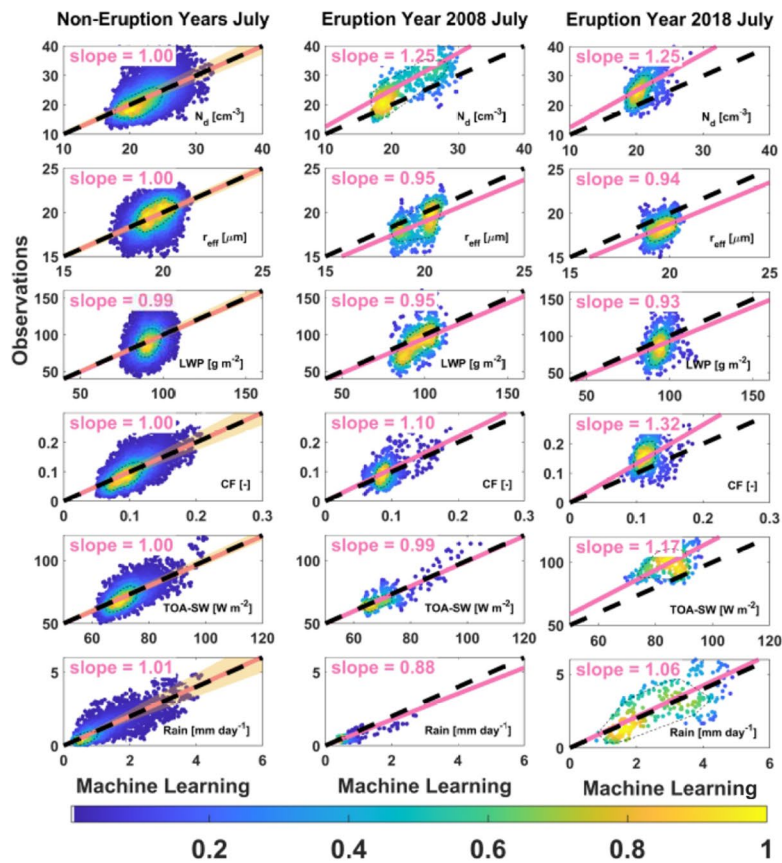
Extended data is available for this paper at <https://doi.org/10.1038/s41561-024-01427-z>.

Supplementary information The online version contains supplementary material available at <https://doi.org/10.1038/s41561-024-01427-z>.

Correspondence and requests for materials should be addressed to Ying Chen.

Peer review information *Nature Geoscience* thanks Hauke Schulz and the other, anonymous, reviewer(s) for their contribution to the peer review of this work. Primary Handling Editor: Tom Richardson, in collaboration with the *Nature Geoscience* team.

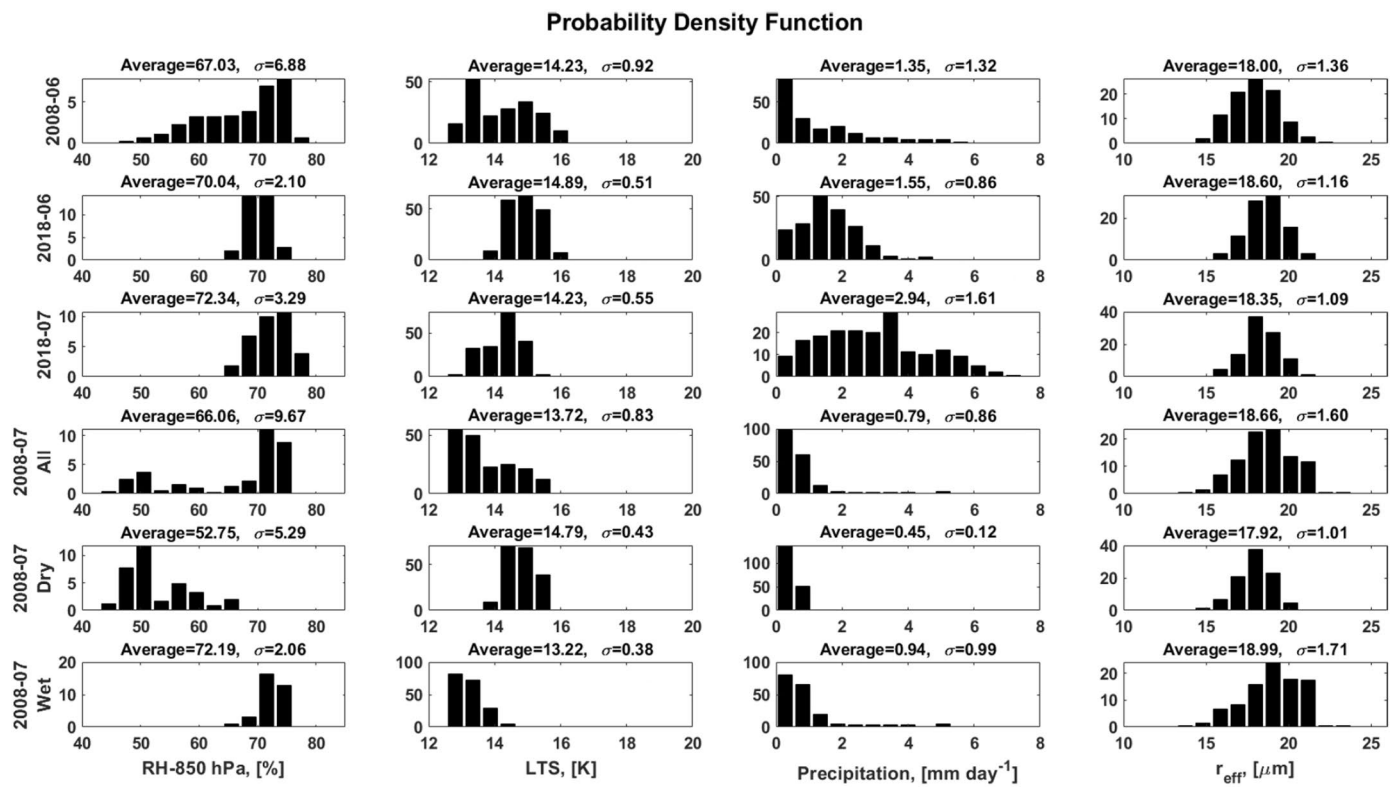
Reprints and permissions information is available at www.nature.com/reprints.

a**b**

Extended Data Fig. 1 | See next page for caption.

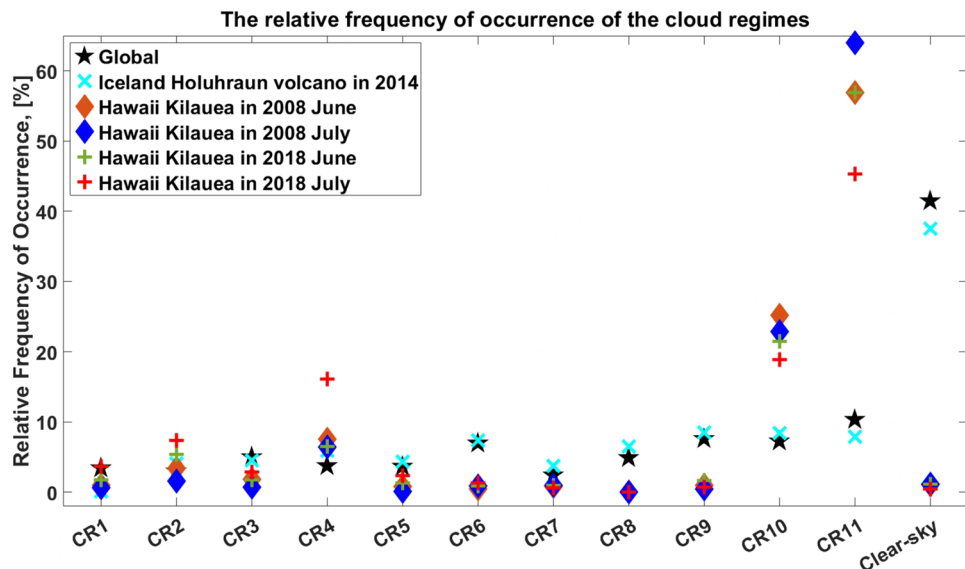
Extended Data Fig. 1 | Validation of machine-learning surrogates against observations. Panel (a) June and (b) July. Left subpanels show validations in non-eruption years, demonstrating the very good agreement between machine-learning surrogates and observations, with regression (pink lines) very close to the 1:1 black lines and 80% of the data (black dash circles) around the 1:1 lines. The shading areas indicate the 90% confidence interval for the multi-year regression lines based on individual years. The middle subpanels show results for the eruption year 2008 and the right subpanels show results for the eruption year 2018, highlighting the differences between machine-learning surrogates and observations. The following variables are shown from top to bottom: cloud

droplet number concentration (N_d), cloud droplet effective radius (r_{eff}), in-cloud liquid water path (LWP), cloud fraction (CF, or cloud cover), reflected shortwave radiation (SW) at the top of the atmosphere (TOA), and daily precipitation (Rain). The colour of each pixel indicates the normalized data density function, brighter colour means more data points in this pixel. A steeper pink slope (than the black dashed line) indicates an increase of the given variable compared to the non-eruption years average. Note that the slopes here can be different from the ratios in Fig. 2, in which area-weighted averaging is applied and provides a more robust validation using Monte Carlo bootstrapping.



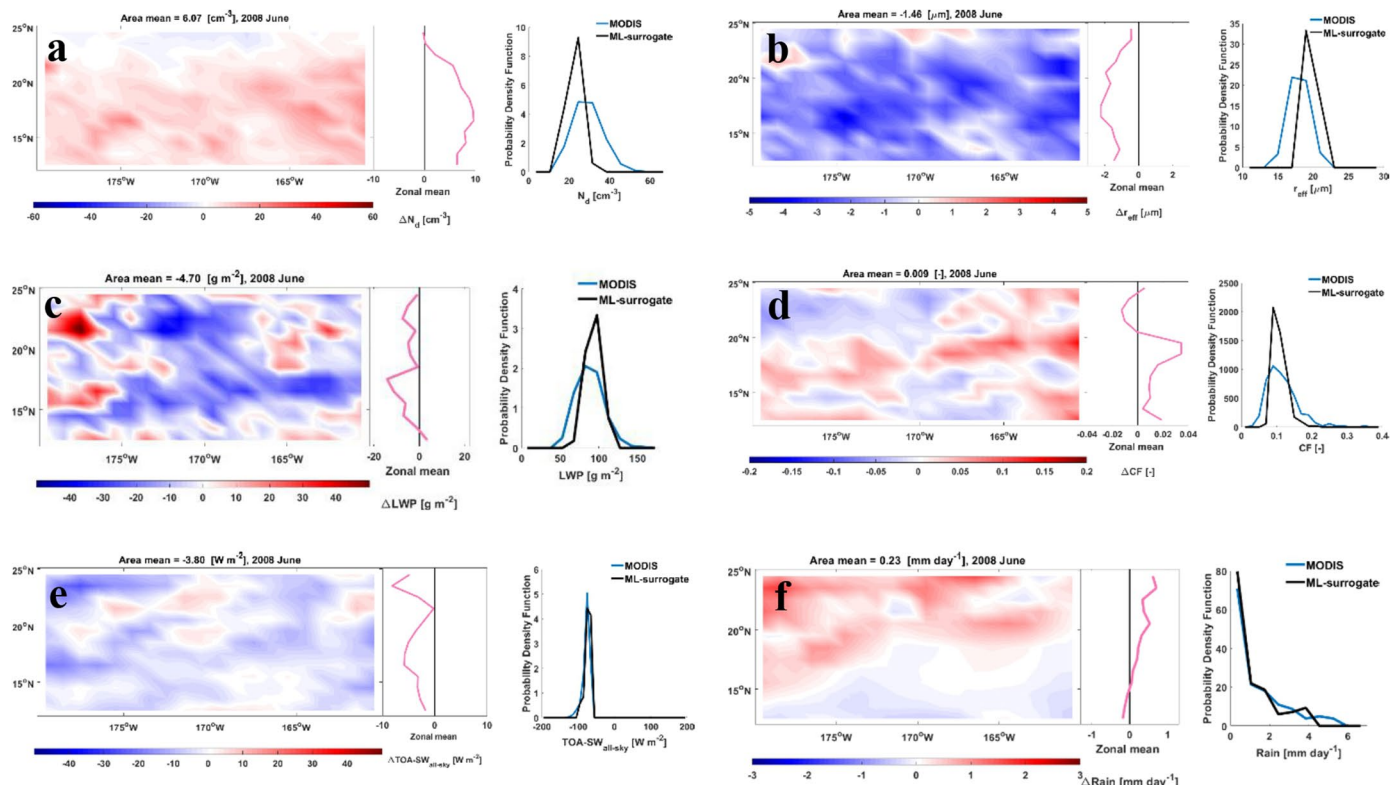
Extended Data Fig. 2 | Probability density function of meteorological and cloud properties in each case. Bar charts of the probability distribution is shown in the bar chart, with average and standard deviation marked on the top. Relative humidity (RH) > 75% indicates very humid condition, RH < 50% indicates

very dry conditions³³; lower-tropospheric stability (LTS) < 14 K indicates unstable conditions, and cloud droplet effective radius (r_{eff}) > 14 μm indicates precipitating clouds¹⁷.



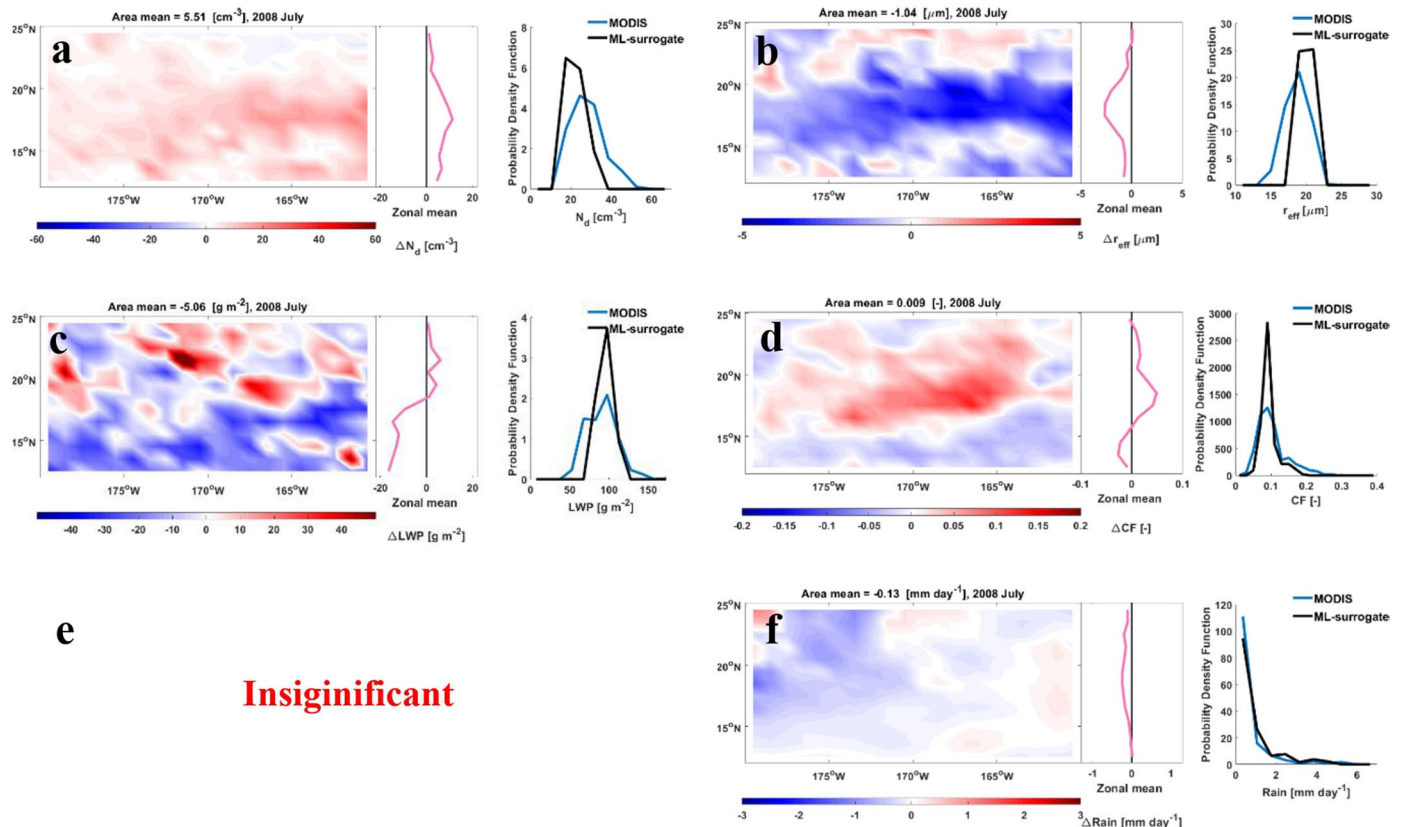
Extended Data Fig. 3 | Spectrum of cloud regime (CR) relative frequency of occurrence. CR10 represents shallow oceanic convective clouds, and CR11 represents small broken clouds with small cloud fraction. The studied region is mainly dominated by the CR10-11. Short description of other CRs: CR1 – tropical deep convection; CR2 – tropical anvils and cirrus; CR3 – tropical and

mid-latitude convection; CR4 – mid-latitude and subtropical high clouds; CR5 – storms; CR6 – midlevel clouds; CR7 – thick high stratus; CR8 – thick low stratus; CR9 – oceanic stratocumulus. More details and original data of cloud regimes please refer to ref. 66.



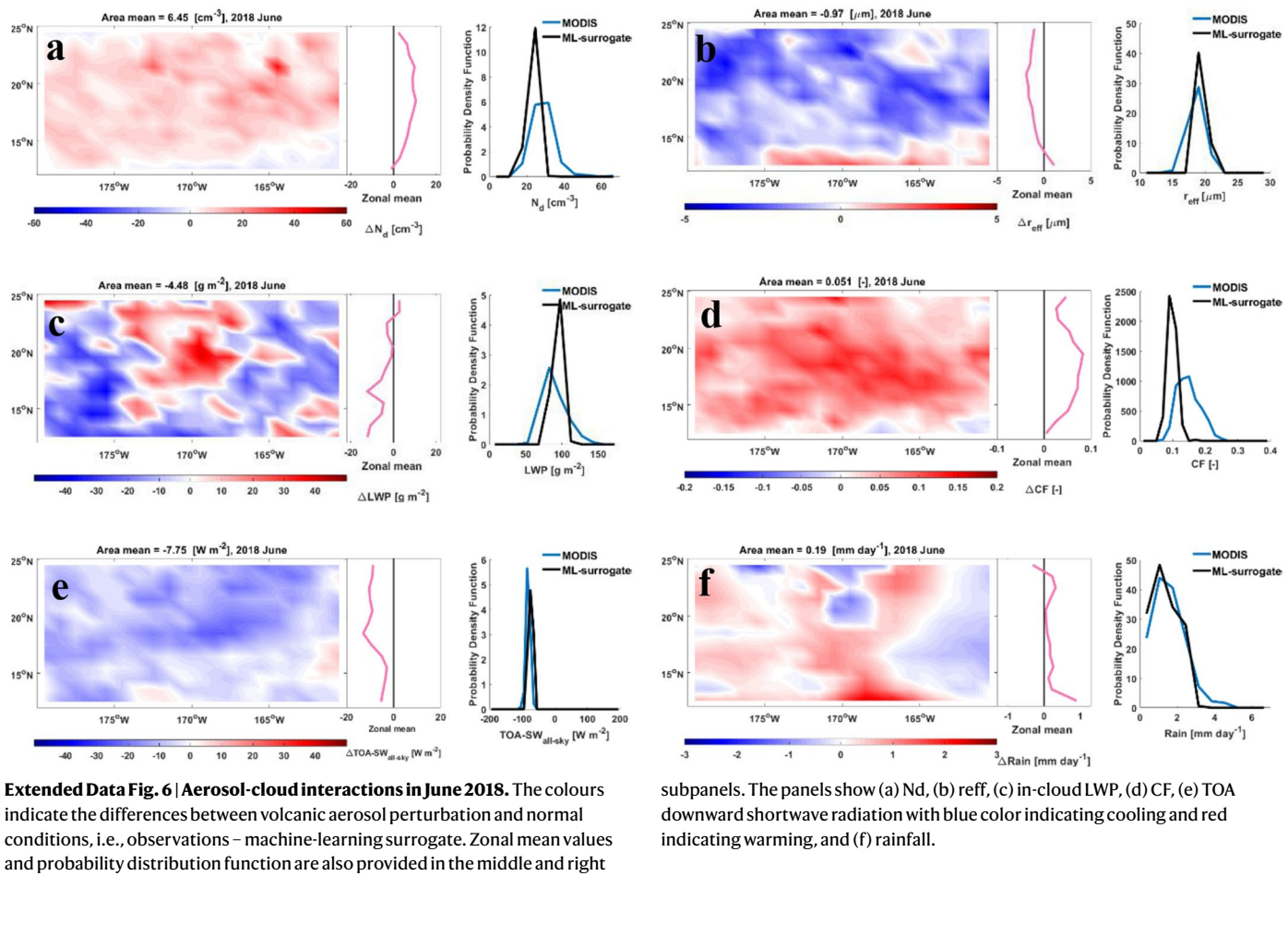
Extended Data Fig. 4 | Aerosol-cloud interactions in June 2008. The colours indicate the differences between volcanic aerosol perturbation and normal conditions, that is, observations – machine-learning surrogate. Zonal mean values and probability distribution function are also provided in the middle

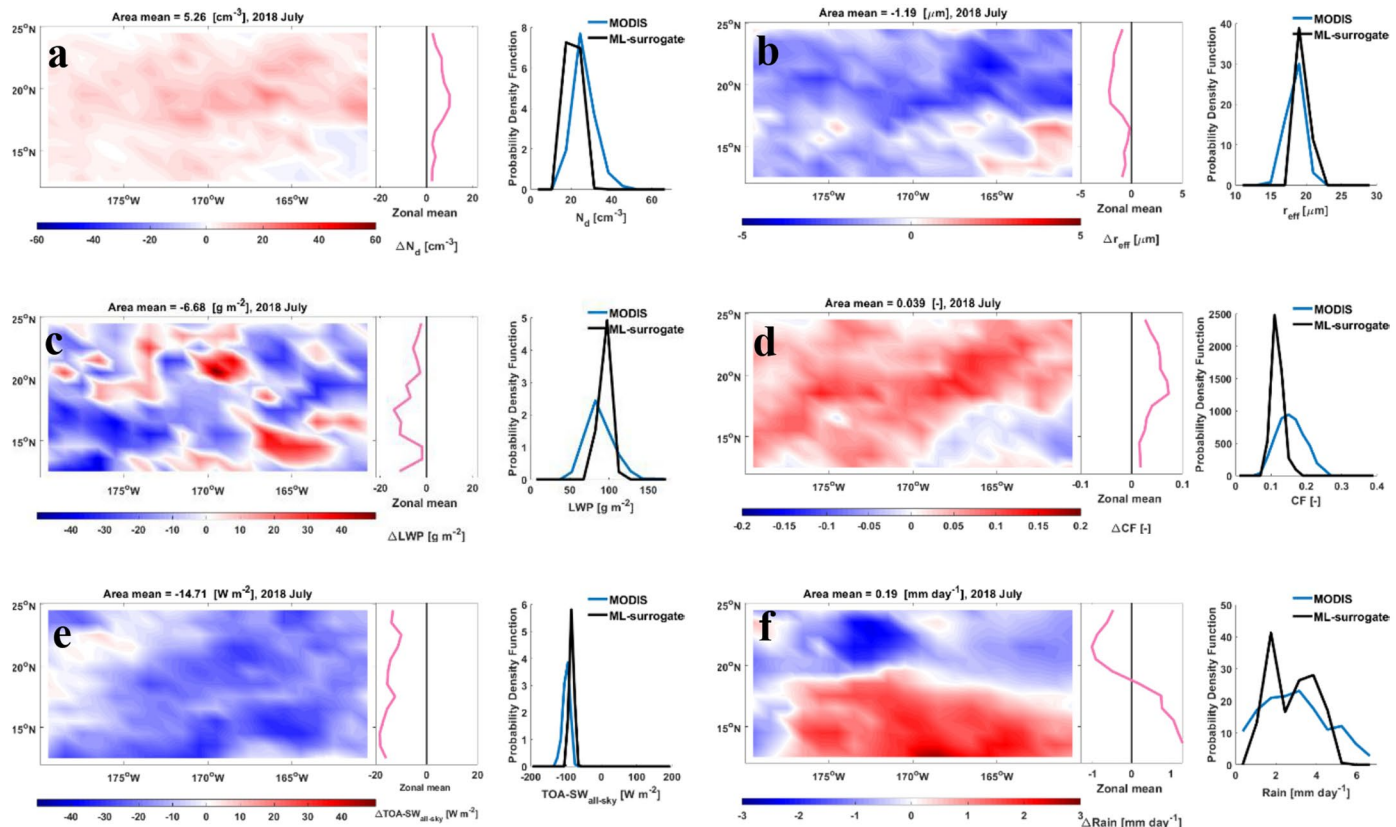
and right subpanels. The panels show (a) N_d , (b) r_{eff} , (c) in-cloud LWP, (d) CF, (e) TOA downward shortwave radiation with blue colour indicating cooling and red indicating warming, and (f) rainfall.



Extended Data Fig. 5 | Aerosol-cloud interactions in July 2008. The colours indicate the differences between volcanic aerosol perturbation and normal conditions, i.e., observations – machine-learning surrogate. Zonal mean values and probability distribution function are also provided in the middle and right

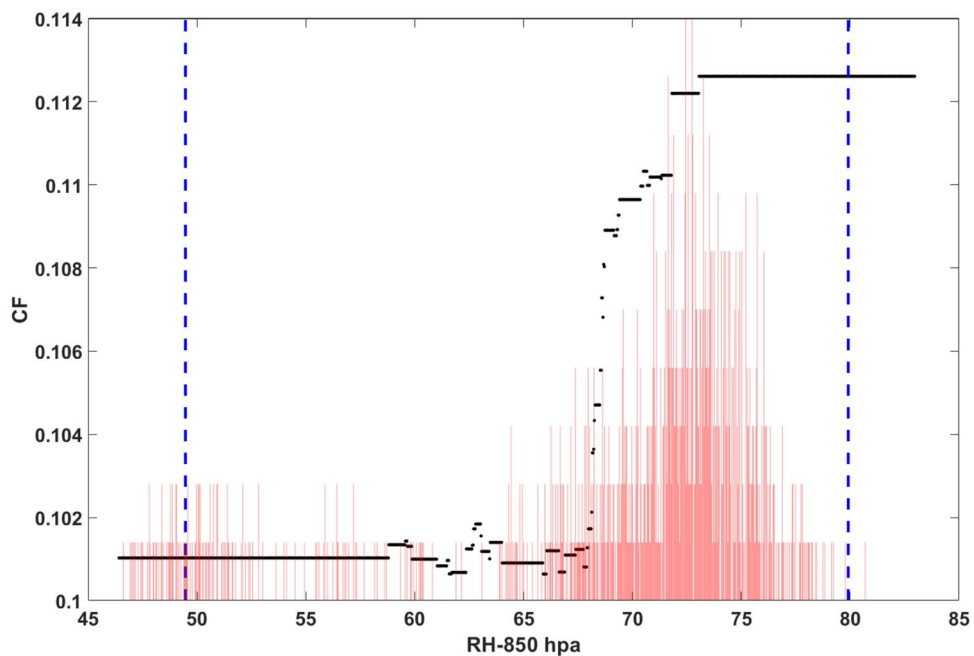
subpanels. The panels show (a) ΔN_d , (b) Δr_{eff} , (c) in-cloud LWP, (d) CF, (e) TOA downward shortwave radiation, does not pass the significance test and therefore is marked as “insignificant”, and (f) rainfall.





Extended Data Fig. 7 | Aerosol-cloud interactions in July 2018. The colours indicate the differences between volcanic aerosol perturbation and normal conditions, i.e., observations – machine-learning surrogate. Zonal mean values and probability distribution function are also provided in the middle and right

subpanels. The panels show (a) Nd, (b) reff, (c) in-cloud LWP, (d) CF, (e) TOA downward shortwave radiation with blue color indicating cooling and red indicating warming, and (f) rainfall.



Extended Data Fig. 8 | Partial dependence of cloud fraction (CF, also known as cloud cover) on 850 hPa RH. The other predictors are fixed at average values. The RH range of the training dataset is marked with blue dash lines, and the probability distribution of RH in July 2008 is indicated by the red bars.